



# High-performance, stable buffer-layer-free $\text{La}_{0.9}\text{Sr}_{0.1}\text{Ga}_{0.8}\text{Mg}_{0.2}\text{O}_3$ electrolyte-supported solid oxide cell with a nanostructured nickel-based hydrogen electrode

Jiaqi Qian<sup>a</sup>, Changgen Lin<sup>a</sup>, Zhiyi Chen<sup>a</sup>, Jiongyuan Huang<sup>a</sup>, Na Ai<sup>b</sup>, San Ping Jiang<sup>c,d</sup>, Xiaoliang Zhou<sup>e</sup>, Xin Wang<sup>a</sup>, Yanqun Shao<sup>a</sup>, Kongfa Chen<sup>a,\*</sup>

<sup>a</sup> College of Materials Science and Engineering, Fuzhou University, Fuzhou, Fujian 350108, China

<sup>b</sup> Fujian College Association Instrumental Analysis Center, Fuzhou University, Fuzhou, Fujian 350108, China

<sup>c</sup> Foshan Xianhu Laboratory of the Advanced Energy Science and Technology Guangdong Laboratory, Foshan, Guangdong 528216, China

<sup>d</sup> WA School of Mines: Minerals, Energy and Chemical Engineering, Curtin University, Perth, WA 6102, Australia

<sup>e</sup> College of Chemistry and Chemical Engineering, Southwest Petroleum University, Chengdu 610500, China

## ARTICLE INFO

### Keywords:

Sintering-free  
Buffer-layer-free  
Nanostructure  
Interface formation  
Elemental interdiffusion

## ABSTRACT

$\text{La}_{0.9}\text{Sr}_{0.1}\text{Ga}_{0.8}\text{Mg}_{0.2}\text{O}_3$  (LSGM) with an extraordinary oxygen-ion conductivity has been extensively studied as an electrolyte material for intermediate temperature solid oxide cells (SOCs). However, the conventional high-temperature sintering process of electrodes results in detrimental reaction between LSGM and Ni-based hydrogen electrode and microstructural coarsening of the electrode. Herein, a buffer-layer-free LSGM electrolyte-supported single cell with a nanostructured Ni-Gd<sub>0.1</sub>Ce<sub>0.9</sub>O<sub>1.95</sub> (GDC) electrode is developed using a sintering-free fabrication approach. The cell exhibits a peak power density of 1.23 W cm<sup>-2</sup> at 800 °C and an electrolysis current density of 1.85 A cm<sup>-2</sup> at 1.5 V with excellent operating stability. The good performance and durability is owing to the synergistic effects of the elimination of elemental interdiffusion at the electrode/electrolyte interface, polarization induced in situ formation of hetero-interfaces between Ni-GDC and LSGM, and remarkable structural stability of Ni-GDC. This study provides an innovative means for the development of efficient and durable buffer-layer-free LSGM-supported SOC.

## 1. Introduction

As the supply of fossil fuels continues to decline, the efficient utilisation and storage of renewable energy have played an increasingly important role. Solid oxide cells (SOCs) are a promising electrochemical energy conversion and storage device operating at elevated temperatures that allow good catalytic activity of non-precious metals and oxides [1,2]. The most common hydrogen electrode material is Ni-based cermet, and perovskite oxides such as  $\text{La}_{0.75}\text{Sr}_{0.25}\text{Cr}_{0.5}\text{Mn}_{0.5}\text{O}_3$  and  $\text{Sr}_{2}\text{Fe}_{1.5}\text{Mo}_{0.5}\text{O}_{6-\delta}$  have also been actively explored as a potential hydrogen electrode [3–7]. Fluorite oxide yttria-stabilized zirconia (YSZ) has been the state-of-the-art electrolyte material for high-temperature SOC (>800 °C), but its oxygen-ion conductivity is inadequate at intermedium temperatures (600–800 °C) [8]. In contrast, perovskite oxide  $\text{La}_{0.9}\text{Sr}_{0.1}\text{Ga}_{0.8}\text{Mg}_{0.2}\text{O}_3$  (LSGM) possesses a much higher oxygen-ion conductivity than YSZ (0.12 vs 0.05 S cm<sup>-1</sup> at 800 °C), and

therefore, LSGM has been widely studied as a candidate electrolyte material for intermediate-temperature SOC [9–11].

The conventional high-temperature sintering process of electrodes at above 1100 °C can result in detrimental reaction between LSGM electrolyte and Ni-based hydrogen electrode and significant microstructural coarsening of the electrode. A buffer layer is generally introduced between the LSGM and Ni-based electrode to avoid the elemental interdiffusion and formation of insulated secondary phases during high-temperature sintering [12,13]. The commonly used buffer layer material is doped CeO<sub>2</sub>, of which La-doped CeO<sub>2</sub> (LDC) has been demonstrated to effectively avoid the generation of massive secondary phases between the buffer layer and LSGM [14–16]. However, the oxygen-ion conductivity of LDC is relatively low and a recent report showed that LDC reacts with LSGM to form a certain amount of secondary phases [17]. An alternative way to avoid the interfacial interaction and microstructural coarsening of hydrogen electrodes is to incorporate the

\* Corresponding author.

E-mail address: [kongfa.chen@fzu.edu.cn](mailto:kongfa.chen@fzu.edu.cn) (K. Chen).

<https://doi.org/10.1016/j.apcatb.2024.123742>

Received 17 October 2023; Received in revised form 11 January 2024; Accepted 14 January 2024

Available online 15 January 2024

0926-3373/© 2024 Elsevier B.V. All rights reserved.

Ni phase into pre-sintered porous LSGM scaffolds by infiltration [18–21]. The relatively low heat-treatment temperature of infiltrated electrodes not only avoids the chemical reaction between Ni and LSGM, but also creates a highly active nanostructure. For instance, Han et al. constructed symmetrical porous LSGM scaffolds where nanoscale Ni-Sm doped  $\text{CeO}_2$  (SDC) and  $\text{SmBa}_{0.5}\text{Sr}_{0.5}\text{Co}_2\text{O}_5$  catalysts were subsequently infiltrated, achieving a peak power density (PPD) of the single cell as high as  $1.5 \text{ W cm}^{-2}$  at  $600^\circ\text{C}$  [20]. Gao et al. infiltrated Ni nanoparticles into porous  $\text{Sr}_{0.8}\text{La}_{0.2}\text{TiO}_3$ /LSGM bilayer scaffolds that acted as a mechanical support for a LSGM film and the single cell achieved a PPD of  $1.1 \text{ W cm}^{-2}$  at  $650^\circ\text{C}$  [21]. However, the relevant reports regarding the durability of the Ni infiltrated LSGM hydrogen electrodes are scarce, probably owing to the fact that the lack of strong interaction between the infiltrated nanoparticles and scaffolds can lead to significant microstructural coarsening and thereby poor operating stability of the electrodes [22].

Herein, we report the development a buffer-layer-free LSGM electrolyte-supported single cell with a nanostructured Ni-Gd doped  $\text{CeO}_2$  (GDC) hydrogen electrode using a sintering-free fabrication approach developed by our group [23–25]. The no necessity of high-temperature sintering step with this approach not only prevents the interfacial reaction between the Ni-GDC and LSGM, but also enables the preservation of the original ultrafine microstructure of the source powder in the hydrogen electrode. More importantly, remarkable microstructural integrity of the nanostructured Ni-GDC electrode can be expected owing to the pre-construction of strong metal–oxide interaction in the source powder [26]. The results show that the buffer-layer-free LSGM electrolyte-supported single cell with the nanostructured Ni-GDC hydrogen electrode achieves good output performance and durability.

## 2. Experimental

Buffer-layer-free electrolyte-supported single cells with a structure of  $\text{NiO-Gd}_{0.1}\text{Ce}_{0.9}\text{O}_{1.95}$  (GDC)| $\text{La}_{0.9}\text{Sr}_{0.1}\text{Ga}_{0.8}\text{Mg}_{0.2}\text{O}_3$  (LSGM)| $\text{La}_{0.6}\text{Sr}_{0.4}\text{Co}_{0.2}\text{Fe}_{0.8}\text{O}_{3-\delta}$  (LSCF) were prepared. The NiO-GDC (7:3 in mass ratio) composite powder was synthesized using a modified Pechini method and annealed at  $1000^\circ\text{C}$  for 3 h [26]. The LSCF powder was purchased from Ningbo SOFCMAN Energy Technology Co Ltd. The electrode slurry was obtained by mechanically mixing the electrode powder, terpineol (99.5%), and ethyl cellulose (99.5%) for 2 h. The electrode powder accounted for 60 wt% of the slurry, and the mass ratio of terpineol to ethyl cellulose was 96:4. LSGM electrolyte discs were

prepared by tape casting using  $\text{La}_2\text{O}_3$  (99.99%),  $\text{SrCO}_3$  (99.0%),  $\text{Ga}_2\text{O}_3$  (99.99%), and  $\text{MgO}$  (99.99%) as raw materials, and dense discs in a diameter of 11 mm and a thickness of  $190 \mu\text{m}$  were obtained by sintering at  $1450^\circ\text{C}$  for 10 h. The electrode slurries were applied to both sides of the electrolyte discs by screen-printing with the active area of  $0.22 \text{ cm}^2$ , followed by drying at  $150^\circ\text{C}$  for 1 h. The sintering-free electrode preparation process, which is schematically illustrated in Fig. 1, is much more simplified as compared to the conventional process via high-temperature sintering, of which a LDC buffer layer is generally required. A Pt paste (Gwent Electronic Materials Ltd) was applied to the outer surface of the electrodes as a current collector. The use of Pt as current collector is attributed to its good thermal stability, and it has almost no contribution to the electrocatalytic activity of the electrodes in this study as validated using an Au current collector (Fig. S1). In addition, our previous studies have shown that the electrode/Pt interfaces have a very small contribution to the ohmic resistance of single cells [27,28].

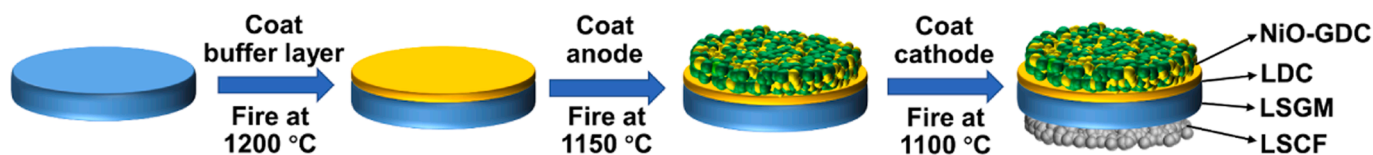
The electrochemical impedance spectra (EIS) and  $I$ - $V$  and  $I$ - $P$  curves of the single cells were measured using an electrochemical workstation (Gamry Interface 1000E) at  $600$ – $800^\circ\text{C}$ . The EIS curves were tested in a frequency range from  $10^5 \text{ Hz}$  to  $10^{-1} \text{ Hz}$  at an AC voltage of  $10 \text{ mV}$ . The operating stability was performed at  $750^\circ\text{C}$ ,  $0.5 \text{ A cm}^{-2}$  using another electrochemical workstation (Arbin BT-2000), with 3 vol%  $\text{H}_2\text{O}$  humidified  $\text{H}_2$  supplied to the hydrogen electrode at a flow rate of  $50 \text{ sccm}$ . The electrolysis was tested at  $700$ – $800^\circ\text{C}$  with a mixture of  $\text{CO}_2$  and  $\text{H}_2$  (volume ratios of 5:5 and 7:3) flowed to the hydrogen electrode at a total flow rate of  $100 \text{ sccm}$ . The EIS curves of LSCF|LSGM|LSCF symmetrical half cells were also measured as a function oxygen partial pressure ( $0.01$ – $0.8 \text{ atm}$ ) at  $800^\circ\text{C}$ . Distribution of relaxation time (DRT) analyses based on the EIS data were obtained using DRT tools with the regularization parameter set at  $10^{-3}$  [29,30].

The morphologies at the interfacial regions between the hydrogen electrode and electrolyte before and after the galvanostatic stability tests were conducted by scanning electron microscopy (SEM, Carl Zeiss SUPRA 55). A lamella sample was obtained at the interface between the hydrogen electrode and electrolyte using focused ion beam-SEM (Helios G4 CX). The morphological and elemental analyses of the lamella were performed by scanning transmission electron microscopy (STEM, Talos F200i) combined with an energy dispersive spectrometer (EDS).

## 3. Results and discussion

Fig. 2 shows the morphologies and electrochemical performance of

### (a) Conventional LSGM-supported cell with sintered electrodes



### (b) Buffer-layer-free LSGM-supported cell with sintering-free electrodes

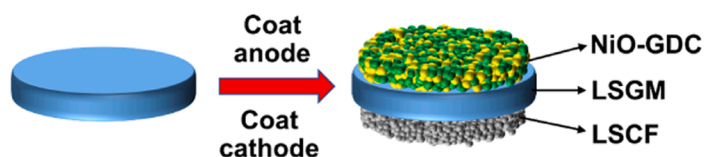
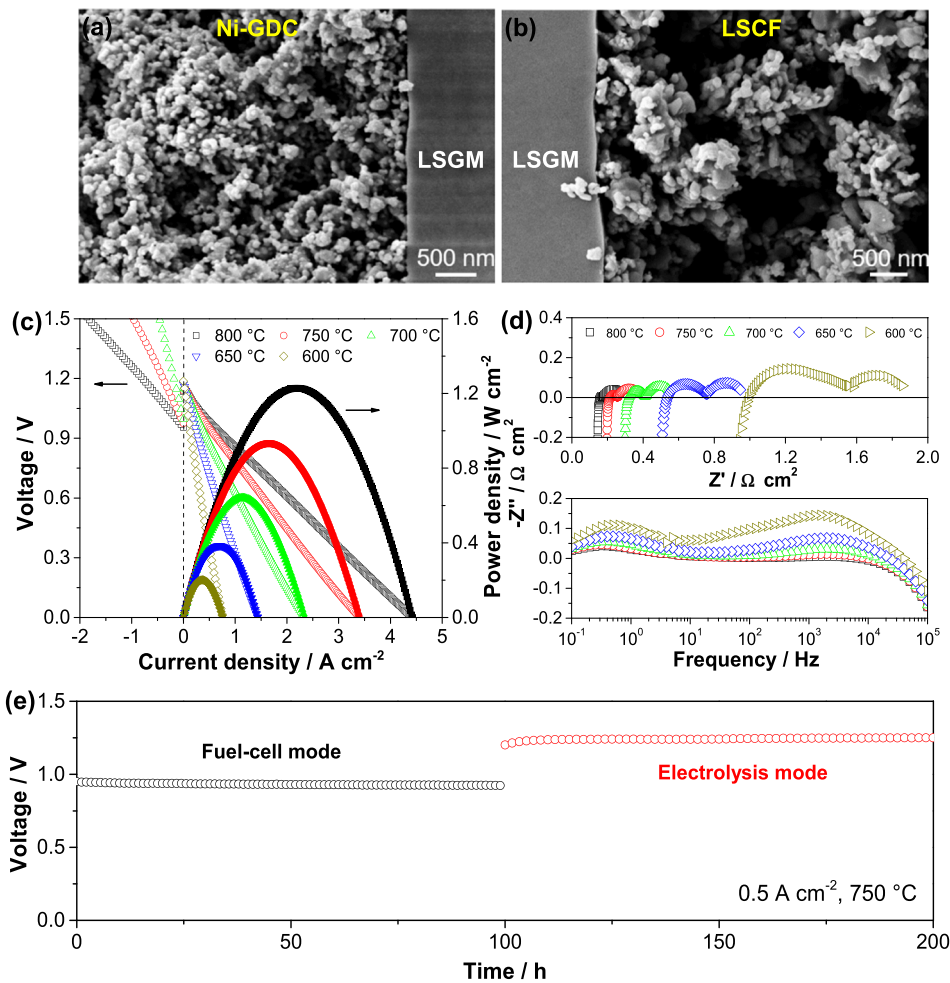


Fig. 1. Flowcharts for the preparation of electrodes of LSGM electrolyte-supported single cells via (a) a conventional high temperature sintering route and (b) a sintering-free route.



**Fig. 2.** SEM images of cross-sections of the Ni-GDC|LSGM|LSCF single cell (a) at the hydrogen electrode side and (b) at the air electrode side. Electrochemical performance and stability of the single cell: (c)  $I$ - $V$  and  $I$ - $P$  curves, (d) Nyquist and Bode plots, and (e) galvanostatic stability testing in the fuel-cell and electrolysis modes at  $0.5 \text{ A cm}^{-2}$ ,  $750^\circ\text{C}$ .

the buffer-layer-free Ni-GDC|LSGM|LSCF single cell. The LSGM electrolyte formed by the in situ solid-state reaction is fully dense without any pinholes (Fig. 2a and b). The freshly prepared sintering-free Ni-GDC and LSCF electrodes possess a nanostructure with a mean particle size of  $75 \pm 34 \text{ nm}$  and  $144 \pm 71 \text{ nm}$  (Fig. S2), respectively. There is certain physical contact at the electrode/electrolyte interfaces (Fig. 2a and b). As the hydrogen electrode is supplied with 3 vol%  $\text{H}_2\text{O}$  humidified  $\text{H}_2$  in the fuel-cell mode, the single cell exhibits PPD of 1.23, 0.93, 0.64, 0.38, and  $0.20 \text{ W cm}^{-2}$  at 800, 750, 700, 650, and  $600^\circ\text{C}$ , respectively (Fig. 2c). As the atmosphere in the hydrogen electrode is switched to

mixed  $\text{CO}_2\text{-H}_2$  (1:1, v/v), the single cell delivers an electrolysis current density of 1.85, 1.01, and  $0.50 \text{ A cm}^{-2}$  @  $1.5 \text{ V}$  at 800, 750, and  $700^\circ\text{C}$ , respectively (Fig. 2c). As the  $\text{CO}_2/\text{H}_2$  ratio increases to 7:3, the electrolysis current density @  $1.5 \text{ V}$  decreases to  $1.63 \text{ A cm}^{-2}$  at  $800^\circ\text{C}$  (Fig. S3). The electrochemical performance of the single cell in this study is among the good ones reported in the literature (Table 1), though the fabrication process of the sintering-free electrodes has yet been optimized. The Nyquist plots show that at 800, 750, 700, 650, and  $600^\circ\text{C}$ , the ohmic resistance ( $R_o$ ) is 0.14, 0.19, 0.31, 0.51, and  $0.98 \Omega \text{ cm}^2$ , and the polarization resistance ( $R_p$ ) is 0.15, 0.19, 0.27, 0.48, and

**Table 1**

Comparison of the PPDs of the single cells with the LSGM electrolyte in the literature and this study.

Hydrogen electrode	Heat-treatment temperature / $^\circ\text{C}$	Buffer layer	Thickness of LSGM / $\mu\text{m}$	Testing temperature / $^\circ\text{C}$	PPD / $\text{W cm}^{-2}$	Ref.
Ni-GDC	/	/	190	800	1.23	This study
Ni-GDC	1150	LDC	300	800	0.98	[31]
Ni-GDC	1350	LDC	250	800	0.85	[32]
Ni-SDC	1200	SDC	500	800	0.55	[10]
Ni-SDC infiltrated LSGM	700	/	9	600	1.50	[20]
Ni infiltrated LSGM	700	/	30	650	1.20	[18]
Ni filtrated LSGM/SLT	700	/	15	650	1.12	[21]
Ni-SDC	1350	SDC	1.47	800	1.08	[33]
Ni-GDC	1300	/	20	700	0.93	[34]
NiFe infiltrated YSZ	1350	CMF/Ti-LDC	50	600	0.95	[35]
NiFe-SDC	1450	SDC	5	800	0.57	[36]

Note: SLT:  $\text{Sr}_{0.8}\text{La}_{0.2}\text{TiO}_3$ ; CMF:  $\text{Ce}_{0.6}\text{Mn}_{0.3}\text{Fe}_{0.1}\text{O}_{2-\delta}$ ; Ti-LDC:  $\text{TiO}_2$  added  $\text{Ce}_{0.6}\text{La}_{0.4}\text{O}_{2-\delta}$ .

$0.95 \Omega \text{ cm}^2$ , respectively (Fig. 2d). This implies that  $R_0$  and  $R_p$  have an almost equal contribution in limiting the output performance of the single cells. As a constant current density of  $0.5 \text{ A cm}^{-2}$  is applied at  $750^\circ\text{C}$ , the cell shows good stability with no noticeable performance degradation for operation in the fuel-cell mode for 100 h and in the electrolysis mode for another 100 h in a  $\text{CO}_2/\text{H}_2$  ratio of 5:5 (Fig. 2e). As the  $\text{CO}_2/\text{H}_2$  ratio increases to 7:3, the single cell shows a certain loss of voltage during the first 20 h galvanostatic electrolysis test, but becomes more or less stable in the rest of test for 100 h (Fig. S3). This demonstrates the good durability of the buffer-layer-free LSGM-supported cell with the nanostructured electrodes. The single cell with a coarsened Ni-GDC electrode sintered at  $1200^\circ\text{C}$  achieves a PPD of  $1.12 \text{ W cm}^{-2}$  at  $800^\circ\text{C}$ , however, its operating stability is not as good as that of the cell with the sintering-free nanostructured Ni-GDC electrode (Fig. S4), probably owing to the reduced metal-oxide interaction on restraining the migration and growth of Ni phase in the sintered Ni-GDC hydrogen electrode [26].

To determine the specific electrode processes of the single cell, EIS curves and DRT analyses were performed at varied temperatures and hydrogen partial pressures, as shown in Fig. 3a, b and Fig. S5. There are four DRT characteristic peaks at high, medium, low, and very low frequencies (HF, MF, LF, and L'F, respectively). The L'F peak is sensitive to the hydrogen partial pressure and it also changes with the temperature (Fig. 3a and b), indicating it is related to the surface reaction at the hydrogen electrode [37]. The LF peak does not change as the temperature decreases and it is insensitive to the hydrogen partial pressure (Fig. 3a and b), indicating that it is likely related to the gas diffusion process in the air electrode [38,39]. A LSCF|LSGM|LSCF symmetrical half cell was also tested under varied oxygen partial pressures (Fig. 3c and Fig. S6), and three DRT peaks appear in the identical characteristic frequencies to the HF, MF, and LF peaks of the single cell. As shown by the deconvoluted  $R_p$  derived at different oxygen partial pressures, the fitted  $n$  values of the HF, MF, and LF processes are 0.01, 0.47, and 0.95,

respectively (Fig. S7). Therefore, for the Ni-GDC|LSGM|LSCF single cell, the L'F peak is dominated by the surface reaction at the hydrogen electrode, the LF peak is associated with the gas diffusion at the air electrode, the MF peak is related to the adsorption/dissociation processes at the air electrode, and the HF peak is corresponded to the oxygen ion migration at the air electrode/electrolyte interface [40–42]. According to the fitting results,  $R_p$  of the single cell is mainly dominated by the surface reaction at the hydrogen electrode at  $800$  and  $750^\circ\text{C}$ , while the adsorption/dissociation processes at the air electrode become overwhelming at  $700^\circ\text{C}$  and  $650^\circ\text{C}$  (Fig. 3d and Table S1).

To explore whether the elemental interdiffusion occurs between the Ni-GDC electrode and LSGM electrolyte after the galvanostatic testing in the fuel-cell mode at  $750^\circ\text{C}$  for 100 h, the morphologies and elemental distribution at the Ni-GDC/LSGM interface regions were analysed, as shown in Fig. 4. The STEM image shows that tight contact is formed between the Ni-GDC electrode and electrolyte (Fig. 4a). Elemental mapping and line scans demonstrate that no noticeable elemental interdiffusion occurs at the electrode/electrolyte interface (Fig. 4b–d), indicating that the Ni-GDC and LSGM do not undergo chemical reaction during the period of stability testing. In addition, the GDC (200) and LSGM (022) planes intersect (Fig. 4e), and the Ni (002) and LSGM (110) planes intersect (Fig. 4f). The intersection of these planes indicates the in situ construction of coherent hetero-interfaces between the Ni-GDC and LSGM by passing the polarization current.

To determine the contribution of thermal effect of applied operating temperature on the formation of electrode/electrolyte interface, the Ni-GDC hydrogen electrode was annealed at  $750^\circ\text{C}$  for 100 h under open circuit. The whole annealed Ni-GDC electrode was easily separated from the electrolyte using a sticky tape approach and the exposed electrolyte surface was relatively clean with few electrode particles (Fig. S8a), which is in contrast to the good interfacial bonding of the polarized electrode as examined during forced separation and the presence of a large number of electrode particles on the electrolyte after the

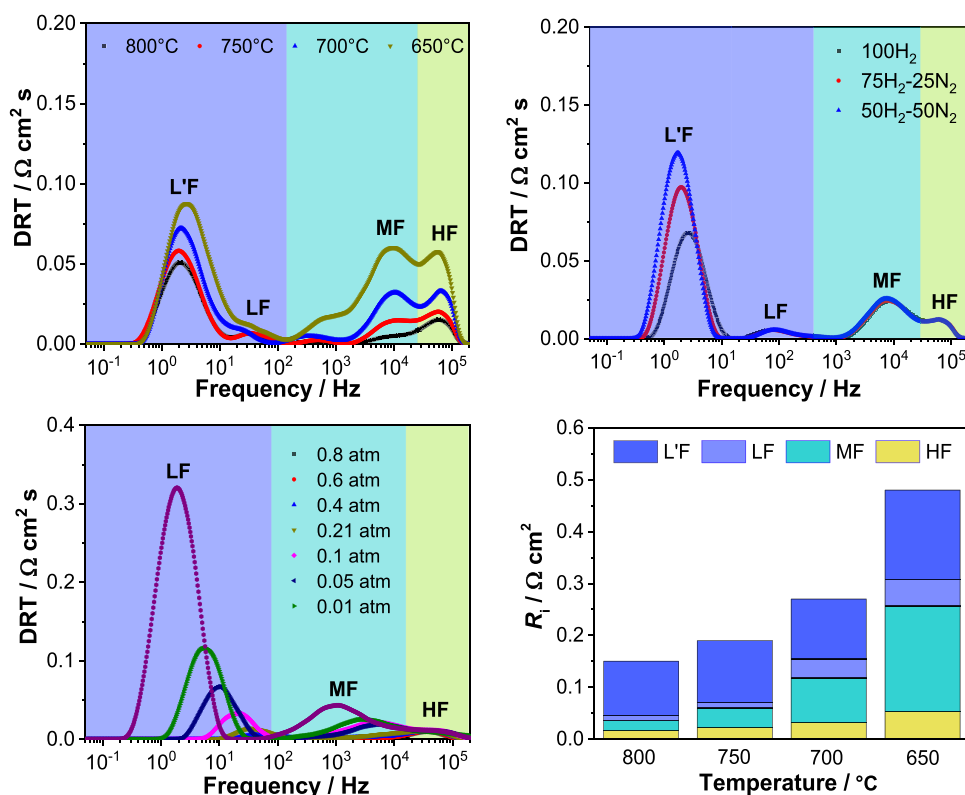


**Fig. 3.** DRT analyses of Ni-GDC|LSGM|LSCF single cell as a function of (a) temperature and (b) hydrogen partial pressure. (c) DRT analyses of LSCF|LSGM|LSCF symmetrical half cell at  $800^\circ\text{C}$  as a function of oxygen partial pressure. (d) Deconvoluted polarization resistances of the single cell as a function of temperature.



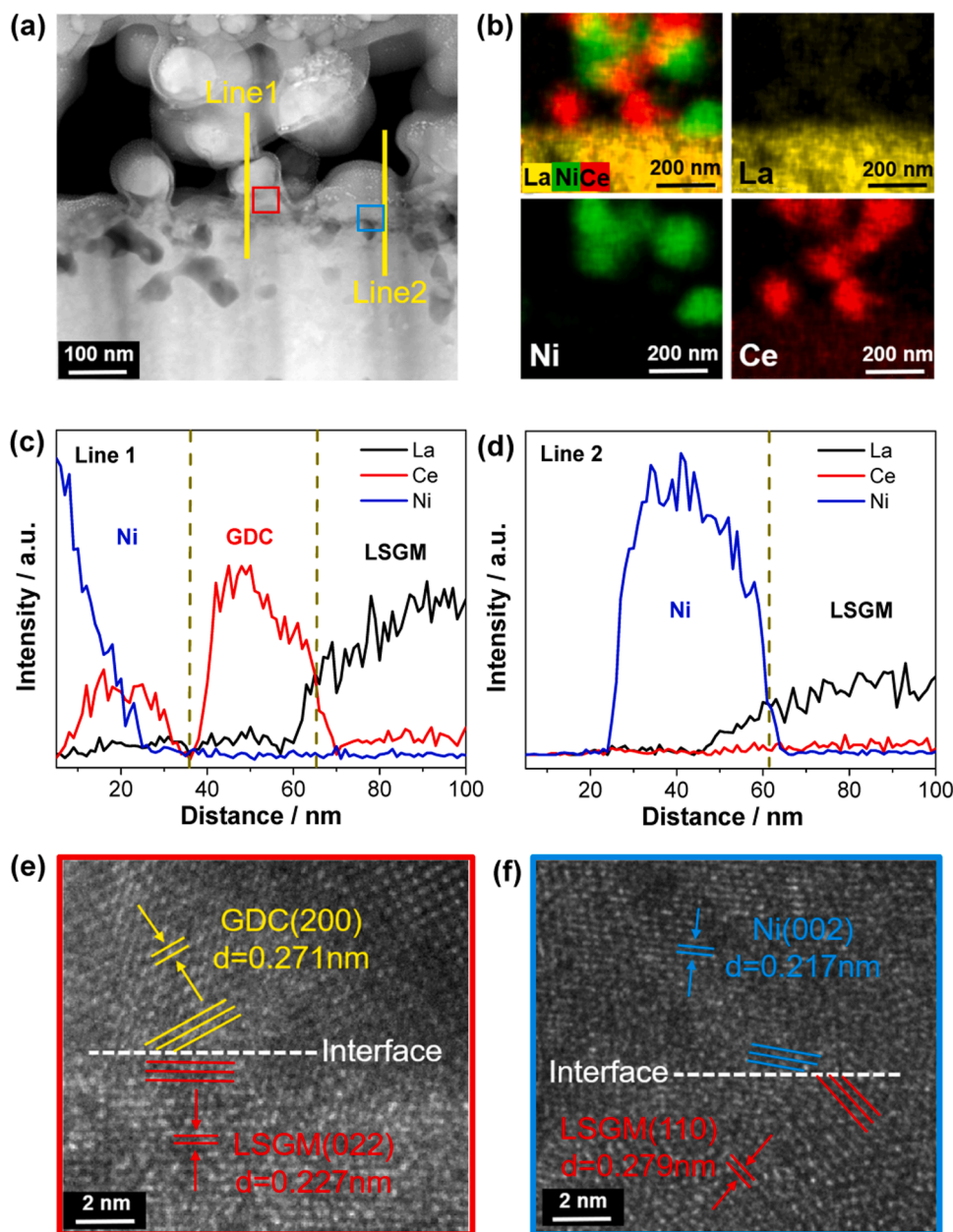


**Fig. 4.** Morphologies and elemental distribution at the Ni-GDC hydrogen electrode/electrolyte interface region after stability testing in the fuel-cell mode at 800 °C for 100 h. (a) STEM image, (b) elemental mapping, (c) elemental scan along line 1, (d) elemental scan along line 2, (e) TEM image of the hetero-interface between GDC and LSGM, and (f) TEM image of the hetero-interface between Ni and LSGM.

galvanostatic test (Fig. S8b). This distinct difference implies that no interaction occurs between the Ni-GDC electrode and LSGM electrolyte during annealing under open-circuit conditions, confirming the dominant role of polarization on constructing the intimate Ni-GDC/LSGM interfaces.

The fundamental mechanism for the interface construction is probably related to the localized sintering effect owing to the release of massive Joule heat during the passage of polarization current through the initially very limited interfaces between the sintering-free Ni-GDC electrode and LSGM electrolyte [26,43]. In theory, the level of Joule heat released is dependent on the extent of interfacial contact and the increase of local temperature can be infinite in the case of very few interfacial contact. Nevertheless, the elimination of elemental interdiffusion at the Ni-GDC/LSGM interface (Fig. 4b and d) in turn implies that the localized interface construction process proceeds very rapidly and the sintering effect is ceased once the hetero-interfaces are formed.

The good durability of the single cell is benefited from not only the elimination of cation interdiffusion at the Ni-GDC electrode/electrolyte interface but also the structural stability of the nanostructured Ni-GDC electrode owing to the strong metal–oxide interaction. The metal–oxide interaction is originally created during the synthesis process of the NiO-GDC composite powder, and the interaction is highly robust regardless of the conversion from NiO to Ni in reducing environment and the galvanostatic testing over an extended period [26]. The strong metal–oxide interaction thus restrains the mobility of the Ni phase and maintains the structural stability of the nanostructured Ni-GDC electrode.

#### 4. Conclusions

In this study, a buffer-layer-free Ni-GDC|LSGM|LSCF single cell has been developed using a sintering-free electrode fabrication approach,

which not only avoids the chemical reaction between the Ni-GDC and LSGM, but also facilitates a highly active nanostructured Ni-GDC electrode. The single cell achieves a peak power density of  $1.23 \text{ W cm}^{-2}$  at  $800^\circ\text{C}$  and an electrolysis current density of 1.85 and  $1.63 \text{ A cm}^{-2}$  at 1.5 V at a  $\text{CO}_2/\text{H}_2$  ratio of 5:5 and 7:3, respectively. The single cell is stable without obvious performance degradation during the galvanostatic testing for 200 h. The good performance and durability of the single cell is owing to the synergistic effects of the elimination of elemental interdiffusion at the hydrogen electrode/electrolyte interface, polarization induced in situ formation of coherent hetero-interfaces between Ni-GDC electrode and LSGM electrolyte, and remarkable structural stability of the nanostructured Ni-GDC electrode. The buffer-layer-free LSGM electrolyte-supported configuration with the sintering-free nanostructured Ni-based hydrogen electrode provides a facile means for the development of efficient and durable SOCs.

## CRediT authorship contribution statement

**Huang Jiongyuan:** Investigation. **Ai Na:** Resources, Methodology. **Lin Changgen:** Investigation. **Chen Zhiyi:** Investigation. **Qian Jiaqi:** Writing – original draft, Investigation, Formal analysis, Data curation. **Chen Kongfa:** Writing – review & editing, Supervision, Funding acquisition, Conceptualization. **Wang Xin:** Data curation. **Shao Yanqun:** Formal analysis. **Jiang San Ping:** Writing – review & editing, Resources. **Zhou Xiaoliang:** Writing – review & editing.

## Declaration of Competing Interest

The authors declare that they have no known competing financial interests or personal relationships that could have appeared to influence the work reported in this paper.

## Data Availability

The authors do not have permission to share data.

## Acknowledgements

The project was supported by National Natural Science Foundation of China (22279018, 22005055, and 21875038) and Natural Science Foundation of Fujian Province (2022J01085).

## Appendix A. Supporting information

Supplementary data associated with this article can be found in the online version at [doi:10.1016/j.apcatb.2024.123742](https://doi.org/10.1016/j.apcatb.2024.123742).

## References

- [1] S.P. Jiang, Solid-state electrochemistry and solid oxide fuel cells: status and future prospects, *Electrochim. Energy Rev.* 5 (2022) 21, <https://doi.org/10.1007/s41918-022-00160-8>.
- [2] A. Hauch, R. Küngas, P. Blennow, A.B. Hansen, J.B. Hansen, B.V. Mathiesen, M. B. Mogensen, Recent advances in solid oxide cell technology for electrolysis, *Science* 370 (2020) 6118, <https://doi.org/10.1126/science.aba6118>.
- [3] S.W. Tao, J.T.S. Irvine, A redox-stable efficient anode for solid-oxide fuel cells, *Nat. Mater.* 2 (2003) 320–323, <https://doi.org/10.1038/nmat871>.
- [4] S.P. Jiang, X.J. Chen, S.H. Chan, J.T. Kwok, GDC-impregnated ( $\text{La}_{0.75}\text{Sr}_{0.25}$ ) ( $\text{Cr}_{0.5}\text{Mn}_{0.5}$ ) $\text{O}_3$  anodes for direct utilization of methane in solid oxide fuel cells, *J. Electrochem. Soc.* 153 (2006) A850, <https://doi.org/10.1149/1.2179347>.
- [5] J. Wan, J.H. Zhu, J.B. Goodenough,  $\text{La}_{0.75}\text{Sr}_{0.25}\text{Cr}_{0.5}\text{Mn}_{0.5}\text{O}_{3-\delta}$ +Cu composite anode running on  $\text{H}_2$  and  $\text{CH}_4$  fuels, *Solid State Ion.* 177 (2006) 1211–1217, <https://doi.org/10.1016/j.ssi.2006.04.046>.
- [6] Q. Liu, X. Dong, G. Xiao, F. Zhao, F. Chen, A novel electrode material for symmetrical SOFCs, *Adv. Mater.* 22 (2010) 5478–5482, <https://doi.org/10.1002/adma.201001044>.
- [7] H. Lv, L. Lin, X. Zhang, Y. Song, H. Matsumoto, C. Zeng, N. Ta, W. Liu, D. Gao, G. Wang, X. Bao, In situ investigation of reversible exsolution/dissolution of CoFe alloy nanoparticles in a Co-doped  $\text{Sr}_2\text{Fe}_{1.5}\text{Mo}_{0.5}\text{O}_{6-\delta}$  cathode for  $\text{CO}_2$  electrolysis, *Adv. Mater.* 32 (2020) 1906193, <https://doi.org/10.1002/adma.201906193>.
- [8] H.G. Shi, C. Su, R. Ran, J.F. Cao, Z.P. Shao, Electrolyte materials for intermediate-temperature solid oxide fuel cells, *Prog. Nat. Sci. -Mater.* 30 (2020) 764–774, <https://doi.org/10.1016/j.pnsc.2020.09.003>.
- [9] T. Ishihara, H. Matsuda, Y. Takita, Doped  $\text{LaGaO}_3$  perovskite type oxide as a new oxide ionic conductor, *J. Am. Chem. Soc.* 116 (1994) 3801–3803, <https://doi.org/10.1021/ja00088a016>.
- [10] K. Huang, R. Tichy, J.B. Goodenough, C. Milliken, Superior perovskite oxide-ion conductor; strontium- and magnesium-doped  $\text{LaGaO}_3$ : III, performance tests of single ceramic fuel cells, *J. Am. Ceram. Soc.* 81 (1998) 2581–2585, <https://doi.org/10.1111/j.1151-2916.1998.tb02664.x>.
- [11] Z. Gao, L.V. Mogni, E.C. Miller, J.G. Railsback, S.A. Barnett, A perspective on low-temperature solid oxide fuel cells, *Energy. Environ. Sci.* 9 (2016) 1602–1644, <https://doi.org/10.1039/c5ee03858h>.
- [12] Z. Salehi, F. Basoli, A. Sanson, E. Mercadelli, S. Licoccia, E. Di Bartolomeo, Porous/dense  $\text{La}_{0.8}\text{Sr}_{0.2}\text{Ga}_{0.8}\text{Mg}_{0.2}\text{O}_{3-\delta}$  (LSGM) bilayer infiltrated with metallic oxidation catalyst, *Ceram. Int.* 40 (2014) 16455–16463, <https://doi.org/10.1016/j.ceramint.2014.07.155>.
- [13] S. Bang, J. Lee, W. Lee, Highly connected oxygen ion conduction pathways in anode functional layer for high performance solid oxide fuel cells, *J. Power Sources* 553 (2023) 232290, <https://doi.org/10.1016/j.jpowsour.2022.232290>.
- [14] M. Hrovat, A. Ahmad-Khanlou, Z. Samardžija, J. Holc, Interactions between lanthanum gallate based solid electrolyte and ceria, *Mater. Res. Bull.* 34 (1999) 2027–2034, [https://doi.org/10.1016/S0025-5408\(99\)00220-2](https://doi.org/10.1016/S0025-5408(99)00220-2).
- [15] K. Huang, J.B. Goodenough, A solid oxide fuel cell based on Sr- and Mg-doped  $\text{LaGaO}_3$  electrolyte: the role of a rare-earth oxide buffer, *J. Alloy. Compd.* 303–304 (2000) 454–464, [https://doi.org/10.1016/S0925-8388\(00\)00626-5](https://doi.org/10.1016/S0925-8388(00)00626-5).
- [16] K.-J. Hwang, M. Jang, M.K. Kim, S.H. Lee, T.H. Shin, Effective buffer layer thickness of La-doped  $\text{CeO}_2$  for high durability and performance on  $\text{La}_{0.9}\text{Sr}_{0.1}\text{Ga}_{0.8}\text{Mg}_{0.2}\text{O}_{3-\delta}$  electrolyte supported type solid oxide fuel cells, *J. Eur. Ceram. Soc.* 41 (2021) 2674–2681, <https://doi.org/10.1016/j.jeurceramsoc.2020.11.036>.
- [17] S. Kumar, A. Chakraborty, S. Kobi, P. Gopalan, T.R.S. Prasanna, Phase formation between  $\text{La}(\text{Sr})\text{Ga}(\text{Mg})\text{O}_3$  and  $\text{Ce}(\text{La})\text{O}_2$  for solid oxide fuel cell applications, *J. Am. Ceram. Soc.* 105 (2022) 3625–3635, <https://doi.org/10.1111/jace.18352>.
- [18] Z. Zhan, D.M. Bierschen, J.S. Cronin, S.A. Barnett, A reduced temperature solid oxide fuel cell with nanostructured anodes, *Energy Environ. Sci.* 4 (2011) 3951–3954, <https://doi.org/10.1039/c1ee01982a>.
- [19] X. Liu, X. Meng, D. Han, H. Wu, F. Zeng, Z. Zhan, Impregnated nickel anodes for reduced-temperature solid oxide fuel cells based on thin electrolytes of doped  $\text{LaGaO}_3$ , *J. Power Sources* 222 (2013) 92–96, <https://doi.org/10.1016/j.jpowsour.2012.08.019>.
- [20] D. Han, H. Wu, J. Li, S. Wang, Z. Zhan, Nanostructuring of  $\text{SmBa}_{0.5}\text{Sr}_{0.5}\text{Co}_2\text{O}_{5+\delta}$  cathodes for reduced-temperature solid oxide fuel cells, *J. Power Sources* 246 (2014) 409–416, <https://doi.org/10.1016/j.jpowsour.2013.07.113>.
- [21] Z. Gao, E.C. Miller, S.A. Barnett, A high power density intermediate-temperature solid oxide fuel cell with thin ( $\text{La}_{0.9}\text{Sr}_{0.1}\text{O}_{0.98}(\text{Ga}_{0.8}\text{Mg}_{0.2})\text{O}_{3-\delta}$ ) electrolyte and nano-scale anode, *Adv. Funct. Mater.* 24 (2014) 5703–5709, <https://doi.org/10.1002/adfm.201400295>.
- [22] S. He, Y. Zou, K. Chen, S.P. Jiang, A critical review of key materials and issues in solid oxide cells, *Interdiscip. Mater.* 2 (2023) 111–136, <https://doi.org/10.1002/idm2.12068>.
- [23] K. Chen, N. Li, N. Ai, Y. Cheng, W.D. Rickard, S.P. Jiang, Polarization-induced interface and Sr segregation of in situ assembled  $\text{La}_{0.6}\text{Sr}_{0.4}\text{Co}_{0.2}\text{Fe}_{0.8}\text{O}_{3-\delta}$  electrodes on  $\text{Y}_2\text{O}_3\text{-ZrO}_2$  electrolyte of solid oxide fuel cells, *ACS Appl. Mater. Interfaces* 8 (2016) 31729–31737, <https://doi.org/10.1021/acsami.6b11665>.
- [24] K. Chen, N. Li, N. Ai, M. Li, Y. Cheng, W.D.A. Rickard, J. Li, S.P. Jiang, Direct application of cobaltite-based perovskite cathodes on the yttria-stabilized zirconia electrolyte for intermediate temperature solid oxide fuel cells, *J. Mater. Chem. A* 4 (2016) 17678–17685, <https://doi.org/10.1039/C6TA07067A>.
- [25] N. Ai, Y. Zou, Z. Chen, K. Chen, S.P. Jiang, Progress on direct assembly approach for in situ fabrication of electrodes of reversible solid oxide cells, *Mater. Rep. Energy* 1 (2021) 100023, <https://doi.org/10.1016/j.matre.2021.100023>.
- [26] B. Wang, Z. Yue, Z. Chen, Y. Zhang, H. Fang, N. Ai, R. Wang, F. Yang, C. Guan, S. P. Jiang, Z. Shao, Y. Luo, K. Chen, Facile construction of nanostructured cermet anodes with strong metal–oxide interaction for efficient and durable solid oxide fuel cells, *Small* 19 (2023) 2304425, <https://doi.org/10.1002/sml.202304425>.
- [27] J. Huang, Z. Xie, N. Ai, C.C. Wang, S.P. Jiang, X. Wang, Y. Shao, K. Chen, A hybrid catalyst coating for a high-performance and chromium-resistive cathode of solid oxide fuel cells, *Chem. Eng. J.* 431 (2022) 134281, <https://doi.org/10.1016/j.cej.2021.134281>.
- [28] J. Huang, Q. Liu, S.P. Jiang, L. Zhao, N. Ai, X. Wang, Y. Shao, C. Guan, H. Fang, Y. Luo, K. Chen, Promotional role of  $\text{BaCO}_3$  on the chromium-tolerance of  $\text{La}_{0.6}\text{Sr}_{0.4}\text{Co}_{0.2}\text{Fe}_{0.8}\text{O}_{3-\delta}$  cathodes of solid oxide fuel cells, *Appl. Catal. B: Environ.* 321 (2023) 122080, <https://doi.org/10.1016/j.apcatb.2022.122080>.
- [29] T.H. Wan, M. Saccoccio, C. Chen, F. Ciucci, Influence of the discretization methods on the distribution of relaxation times deconvolution: implementing radial basis functions with DRTtools, *Electrochim. Acta* 184 (2015) 483–499, <https://doi.org/10.1016/j.electacta.2015.09.097>.
- [30] M. Saccoccio, T.H. Wan, C. Chen, F. Ciucci, Optimal regularization in distribution of relaxation times applied to electrochemical impedance spectroscopy: ridge and lasso regression methods - a theoretical and experimental study, *Electrochim. Acta* 147 (2014) 470–482, <https://doi.org/10.1016/j.electacta.2014.09.058>.
- [31] Z. Yang, C. Yang, B. Xiong, M. Han, F. Chen,  $\text{BaCo}_{0.7}\text{Fe}_{0.2}\text{Nb}_{0.1}\text{O}_{3-\delta}$  as cathode material for intermediate temperature solid oxide fuel cells, *J. Power Sources* 196 (2011) 9164–9168, <https://doi.org/10.1016/j.jpowsour.2011.06.096>.

- [32] L. Shen, Z. Du, Y. Zhang, X. Dong, H. Zhao, Medium-entropy perovskites Sr (Fe<sub>0.4</sub>Ti<sub>0.6</sub>Co<sub>0.4</sub>Mn<sub>0.6</sub>)O<sub>3-δ</sub> as promising cathodes for intermediate temperature solid oxide fuel cell, *Appl. Catal. B-Environ.* 295 (2021) 120264, <https://doi.org/10.1016/j.apcatb.2021.120264>.
- [33] S.-F. Wang, H.-C. Lu, Y.-F. Hsu, P. Jasinski, High-performance anode-supported solid oxide fuel cells with co-fired Sm<sub>0.2</sub>Ce<sub>0.8</sub>O<sub>2-δ</sub>/La<sub>0.8</sub>Sr<sub>0.2</sub>Ga<sub>0.8</sub>Mg<sub>0.2</sub>O<sub>3-δ</sub>/Sm<sub>0.2</sub>Ce<sub>0.8</sub>O<sub>2-δ</sub> sandwiched electrolyte, *Int. J. Hydrog. Energy* 47 (2022) 5429–5438, <https://doi.org/10.1016/j.ijhydene.2021.11.132>.
- [34] J.H. Joo, D.Y. Kim, G.M. Choi, Thick-film electrolyte-supported SOFC based on lanthanum-gallate electrolyte without using buffer layer, *Electrochim. Solid-State Lett.* 12 (2009) B65, <https://doi.org/10.1149/1.3086261>.
- [35] Z. Tan, J.T. Song, A. Takagaki, T. Ishihara, Infiltration of cerium into a NiO–YSZ tubular substrate for solid oxide reversible cells using a LSGM electrolyte film, *J. Mater. Chem. A* 9 (2021) 1530–1540, <https://doi.org/10.1039/D0TA08564B>.
- [36] T. Ishihara, J. Yan, M. Shinagawa, H. Matsumoto, Ni–Fe bimetallic anode as an active anode for intermediate temperature SOFC using LaGaO<sub>3</sub> based electrolyte film, *Electrochim. Acta* 52 (2006) 1645–1650, <https://doi.org/10.1016/j.electacta.2006.03.103>.
- [37] F. Zhang, Q. Weng, Y. Zhang, N. Ai, S.P. Jiang, C. Guan, Y. Shao, H. Fang, Y. Luo, K. Chen, Facile preparation of electrodes of efficient electrolyte-supported solid oxide fuel cells using a direct assembly approach, *Electrochim. Acta* 424 (2022) 140643, <https://doi.org/10.1016/j.electacta.2022.140643>.
- [38] Z. Chen, L. Jiang, S. He, C. Guan, Y. Zou, Z. Yue, N. Ai, S.P. Jiang, Y. Shao, K. Chen, Development of intertwined nanostructured multi-phase air electrodes for efficient and durable reversible solid oxide cells, *Appl. Catal. B-Environ.* 305 (2022) 121056, <https://doi.org/10.1016/j.apcatb.2021.121056>.
- [39] Z. Yue, L. Jiang, Z. Chen, N. Ai, Y. Zou, S.P. Jiang, C. Guan, X. Wang, Y. Shao, H. Fang, Y. Luo, K. Chen, Ultrafine, dual-phase, cation-deficient PrBa<sub>0.8</sub>Ca<sub>0.2</sub>Co<sub>2</sub>O<sub>5+δ</sub> air electrode for efficient solid oxide cells, *ACS Appl. Mater. Inter.* 15 (2023) 8138–8148, <https://doi.org/10.1021/acsami.2c21172>.
- [40] Y. Niu, Y. Zhou, W. Zhang, Y. Zhang, C. Evans, Z. Luo, N. Kane, Y. Ding, Y. Chen, X. Guo, W. Lv, M. Liu, Highly active and durable air electrodes for reversible protonic ceramic electrochemical cells enabled by an efficient bifunctional catalyst, *Adv. Energy Mater.* 12 (2022) 2103783, <https://doi.org/10.1002/aenm.202103783>.
- [41] Y. Zhang, L. Shen, Y. Wang, Z. Du, B. Zhang, F. Ciucci, H. Zhao, Enhanced oxygen reduction kinetics of IT-SOFC cathode with PrBaCo<sub>2</sub>O<sub>5+δ</sub>/Gd<sub>0.1</sub>Ce<sub>1.9</sub>O<sub>2-δ</sub> coherent interface, *J. Mater. Chem. A* 10 (2022) 3495–3505, <https://doi.org/10.1039/D1TA09615J>.
- [42] J.H. Park, C.H. Jung, K.J. Kim, D. Kim, H.R. Shin, J.-E. Hong, K.T. Lee, Enhancing bifunctional electrocatalytic activities of oxygen electrodes via incorporating highly conductive Sm<sup>3+</sup> and Nd<sup>3+</sup> double-doped ceria for reversible solid oxide cells, *ACS Appl. Mater. Interfaces* 13 (2021) 2496–2506, <https://doi.org/10.1021/acsami.0c17238>.
- [43] Z. Chen, L. Jiang, Z. Yue, D. Dong, N. Ai, S.P. Jiang, D. Zhao, X. Wang, Y. Shao, K. Chen, Facile approach for improving the interfacial adhesion of nanofiber air electrodes of reversible solid oxide cells, *ACS Appl. Mater. Interfaces* 15 (2023) 8120–8127, <https://doi.org/10.1021/acsami.2c20974>.